CuN_6 Jahn–Teller centers in coordination frameworks comprising fully condensed Kuratowski-type secondary building units: phase transitions and magneto-structural correlations†

Maciej Grzywa,[a] Dmytro Denysenko,[a] Jan Hanss,[a] Ernst-Wilhelm Scheidt,[b] Wolfgang Scherer,[b] Matthias Weil[c] and Dirk Volkmer*[a]

The metal–organic framework $[Cu(ta)_2]$ (Hta = 1*H*-1,2,3-triazole), containing Jahn–Teller active Cu(II) ions and 1,2,3-triazolate ligands, is prepared under solvothermal reaction conditions. The compound shows a reversible phase transition from the tetragonal crystal system (α-$[Cu(ta)_2]$: space group $I4_1/amd$ (no. 141), a = 11.8447(7) Å, c = 18.9782(13) Å, V = 2662.6(3) Å^3) to the cubic crystal system (β-$[Cu(ta)_2]$: space group $Fd\bar{3}m$ (no. 227), a = 17.4416(15) Å, V = 5305.9(8) Å^3) within the temperature range of 120–160 °C. Both $[Cu(ta)_2]$ polymorphs have identical bonding topologies that might be described as fully condensed Kuratowski-type pentanuclear secondary building units of local T_d point group symmetry in which four Cu(II) ions occupy the vertices of an imaginary tetrahedron. α-$[Cu(ta)_2]$, as opposed to the high-temperature β-phase, shows a strong tetragonal Jahn–Teller distortion of CuN_6 coordination octahedra. The compounds are characterized by elemental and thermogravimetric analyses, single crystal and powder X-ray diffraction, FTIR-, UV-vis and fluorescence spectroscopy. Magnetic susceptibility investigations reveal two different Cu(II) sites at a ratio of 1 : 2, in agreement with the solid state structure of $[Cu(ta)_2]$. At low temperatures the formation of antiferromagnetically coupled Cu(II) dimers is observed, leading to a spin frustration of roughly 1/3 of all magnetically active Cu(II) sites.

Introduction

Metal–organic frameworks (MOFs), which are built up from metal ions or metal-based clusters and organic bridging ligands, have been studied extensively during the past decade owing to their intriguing crystal structures, bonding topologies as well as for their wide range of applications including gas storage[1] and separation,[2] catalysis,[3,4] or controlled drug release.[5] Copper based MOFs have attracted particular interest which relates to the role of copper centres in the active sites of metalloenzymes such as multicopper oxidases and in homogeneous catalysis.[6]

[a]*Institute of Physics, Chair of Solid State and Materials Chemistry, Augsburg University, Universitätstraße 1, 86159 Augsburg, Germany. E-mail: dirk.volkmer@physik.uni-augsburg.de; Fax: +49 (0)821 598-5955; Tel: +49 (0)821 598-3006*
[b]*Institute of Physics, Chair of Chemical Physics and Material Science, Augsburg University, Universitätstraße 1, 86159 Augsburg, Germany. E-mail: wolfgang.scherer@physik.uni-augsburg.de; Fax: +49 (0)821 598-3227; Tel: +49 (0)821 598-3350*
[c]*Institute for Chemical Technologies and Analytics, Division of Structural Chemistry, Vienna University of Technology, Getreidemarkt 9/164-SC, 1060 Vienna, Austria*

† Electronic supplementary information (ESI) available: Atomic coordinates, bond lengths and angles, packing diagrams for α- and β-[Cu(ta)2], XRPD patterns, IR spectrum. CCDC 853111. For ESI and crystallographic data in CIF or other electronic format see DOI: 10.1039/c2dt12311h

Recently, polyaza-heteroaromatic compounds such as pyrazole, imidazole, triazole, tetrazole, as well as their derivatives have emerged as useful ligands in constructing coordination polymers, for which the term metal azolate frameworks (MAFs) has been proposed.[7] Combining polyazolate ligands with late (= electron rich) transition metal ions leads to frameworks with strong and directional metal–nitrogen bonds, providing superior chemical and thermal stability as compared to their carboxylate-based counterparts.[3,8] At present, several reports exist on copper coordination compounds prepared from triazole ligands, most of which employ 1,2,4-triazole and its derivatives. However, Cu(II) coordination compounds containing 1,2,3-triazolates have been less frequently reported so far.[9]

As a part of our long term research on functional MOFs, we have recently reported on 1,2,3-benzotriazolate-based metal complexes comprising "Kuratowski-type" pentanuclear coordination units. These compounds are defined by a particular structural feature: the basic coordination unit shows a central metal ion coordinated by six triazolate ligands spanning a Cartesian system, which can be assembled either into discrete pentanuclear coordination compounds $[MZn_4Cl_4(L)_6]$ (M^{II} = Zn, Fe, Co, Ni, Ru or Cu; L = Me_2bta, 5,6-dimethyl-1,2,3-benzotriazolate)[10] or into 3D porous frameworks such as MFU-4.[11] The graph theoretical analysis proves that the bonding topologies of $[M^{II}Zn_4Cl_4(L)_6]$ units contain the nonplanar $K_{3,3}$ graph. According to a theorem of C. Kuratowski,[12] a finite graph is planar

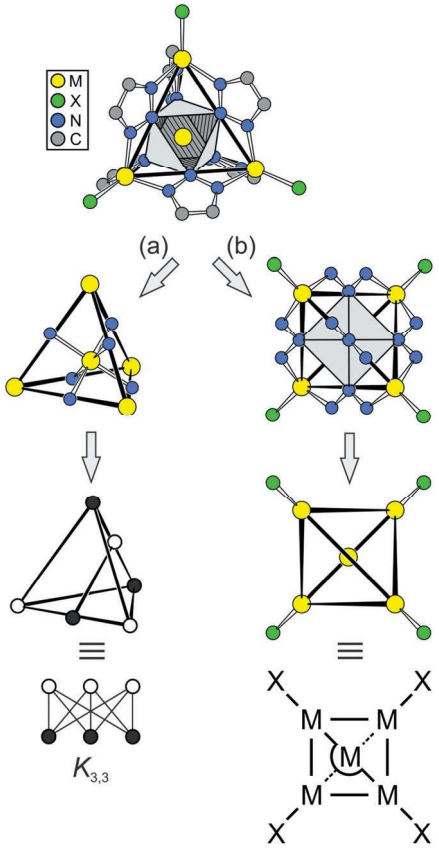

Fig. 1 Structure and bonding scheme of Kuratowski-type coordination compounds. (a) Formal derivation of the $K_{3,3}$ graph which can be used to represent the connectivity in Kuratowski-type coordination compounds. (b) Derivation of a skeletal formula representing discrete $[M_5(X)_4(L)_6)]$ units, where M = metal ion, (X) = mono-, bi- or tridentate capping ligand, and (L) = 1,2,3-triazolate ligand.

if – and only if – it does not contain a subgraph that is a subdivision of K_5 (the complete graph on five vertices) or $K_{3,3}$ (complete bipartite graph on six vertices, three of which connect to each of the other three). As can be seen in Fig. 1, path (a), the molecular graph of $[M^{II}Zn_4Cl_4(L)_6]$ units in fact contains a subgraph of $K_{3,3}$. Consequently there is no possibility to draw a planar graph which leads us to propose a pseudo-perspective skeletal formula as derived in Fig. 1, path (b) to represent Kuratowski-type coordination compounds.

In this article, we report on the synthesis and characterization of a novel MOF compound, $[Cu(ta)_2]$, which represents one among three fundamentally different ways to assemble 3D coordination frameworks from Kuratowski-type secondary building units. In the first network type, represented by the cubic network MFU-4, the μ_3-bridging 1,2,3-triazolate ligands of discrete Kuratowski-SBUs (*cf.* Fig. 1) are replaced by rigid μ_6-bridging bis-triazolate linkers, such as benzo(1,2-d : 4,5-d′) bistriazole H_2-BBTA ($[Zn_5Cl_4(BBTA)_3]$, MFU-4),[11b] or bis-1,2,3-triazolo-([4,5-b],[4′,5′-i])dibenzo-[1,4]-dioxin H_2-BTDD ($[Zn_5Cl_4(BTDD)_3]$, MFU-4*l*).[11a] The second network type is observed in the compound $[M_5(btz)_6(TCNQC)_4(H_2O)_4]\cdot 2H_2O$, (M = Co(II), or Ni(II), btz = 1,2,3-benzotriazolate),[13] where Kuratowski units are interconnected by replacing peripheral ligands X

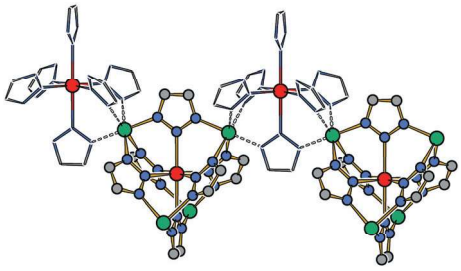

Fig. 2 Excerpt from a coordination polymer composed of $\{Cu_5(ta)_6\}^{4+}$ Kuratowski-type units (shown as ball-and-stick model) and $\{Cu(ta)_6\}^{4-}$ building units (shown as wire model). Cu(II) ions bound to N^2-donor atom of the triazolate ligands are shown in red, Cu(II) ions represented as green spheres are bound to the N^1- or N^3-donor atoms, respectively.

(*cf.* Fig. 1) by μ_2-bridging $TCN\dot{Q}^-$ (7,7,8,8-tetracyano-*p*-quinodimethane) radical anion ligands, giving rise to diamondoid interpenetrated networks. The third framework type is represented by $[Cu(ta)_2]$ reported here, which is formally derived by condensing Kuratowski units $\{Cu_5X_4(ta)_6\}$ with lacunary tetravacant $\{Cu(ta)_6\}^{4-}$ units according to eqn (1) (*cf.* Fig. 2):

$$Cu_5(ta)_6^{4+} + Cu(ta)_6^{4-} \rightarrow Cu_6(ta)_{12} \equiv [Cu(ta)_2] \qquad (1)$$

The Cu(II) centers in these building units show a strong tetragonal Jahn–Teller distortion at room temperature, which vanishes completely upon switching from the tetragonal into the cubic phase within the temperature range of 120–160 °C. The completely reversible phase transition was studied by differential scanning calorimetry and powder diffractometry. The crystal structures of both α- and β-phases of $[Cu(ta)_2]$, its porosity and thermal stability are described. Magnetization and susceptibility investigations support the presence of two different Cu(II) sites in $[Cu(ta)_2]$. In particular, two thirds of the Cu(II) ions lose their magnetic moment at low temperature, which might be ascribed to the formation of antiferromagnetically coupled Cu(II) dimers.

Results and discussion

Synthesis and characterization

Light-blue pseudooctahedral single crystals of α-$[Cu(ta)_2]$ (Fig. 3) were obtained under solvothermal conditions by reacting copper(II) hydroxide with 1*H*-1,2,3-triazole in a $NH_{3(aq)}$–EtOH solution at 120 °C. The compound is insoluble in water, benzene, acetone or chlorobenzene.

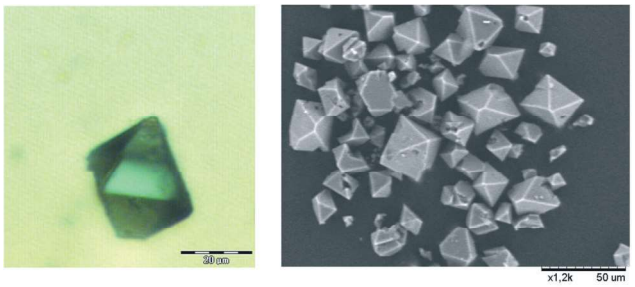

Fig. 3 Optical micrograph (left) and SEM image (right) of the as-synthesized α-$[Cu(ta)_2]$.

Crystal structure analyses

Structure description of α- and β-[Cu(ta)$_2$] phases. Upon heating to $T > 120$ °C, α-[Cu(ta)$_2$] undergoes a reversible first-order endothermic phase transition from a tetragonal into a cubic structure (β-[Cu(ta)$_2$]) which reverts exothermically to the α-phase upon cooling.

Single crystal X-ray structural analysis reveals that α-[Cu(ta)$_2$] crystallizes in the tetragonal crystal system in the space group $I4_1/amd$ (no. 141), while powder X-ray analysis reveals that the β-[Cu(ta)$_2$] phase crystallizes in the cubic crystal system in the space group $Fd\bar{3}m$ (no. 227). The X-ray diffraction studies disclosed β-[Cu(ta)$_2$] to be isostructural with $[Cd_3(ta)_6]\cdot 6H_2O$.[14] The asymmetric unit of α-[Cu(ta)$_2$] contains two copper, four nitrogen, two carbon and two hydrogen atoms, whereas two copper, two nitrogen, one carbon and one hydrogen atoms are found in the asymmetric unit of β-[Cu(ta)$_2$]. Ortep style plots of the asymmetric units of α- and β-[Cu(ta)$_2$] with atom labels are shown in Fig. 4.

As shown in Fig. 5, α- and β-[Cu(ta)$_2$] comprise coordination units, in which the Cu(II) metal ions are coordinated by six tridentate triazolate ligands *via* nitrogen donor atoms. In α-[Cu(ta)$_2$] the d^9 Cu(II) ions are placed in CuN_6 octahedra which show two different kinds of tetragonal distortion. The Cu1 centers, placed at sites with 2/*m* symmetry, have four equal

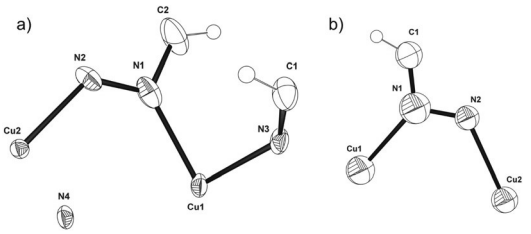

Fig. 4 View of the asymmetric units of α-[Cu(ta)$_2$] (a) and β-[Cu(ta)$_2$] (b) showing the atom numbering scheme. Displacement ellipsoids are drawn at the 50% probability level.

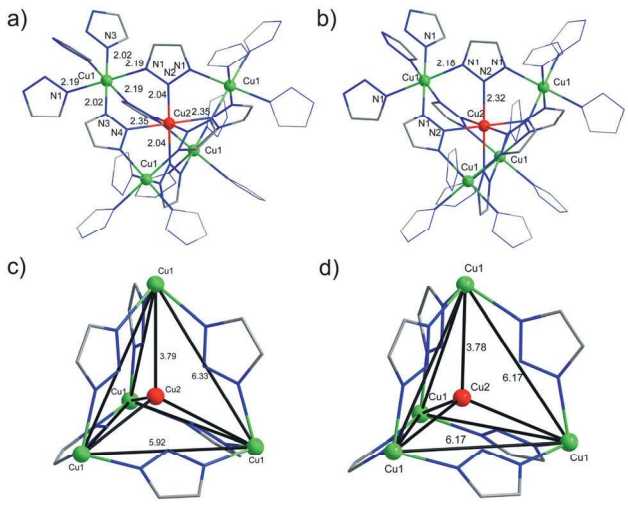

Fig. 5 Selected bond distances in the coordination units of α-[Cu(ta)$_2$] (a) and β-[Cu(ta)$_2$] (b); non-bonding Cu–Cu distances represented by imaginary tetrahedra (black lines) in α- (c) and β-[Cu(ta)$_2$] (d).

Table 1 Selected distances (Å) for compounds α- and β-[Cu(ta)$_2$]

α-[Cu(ta)$_2$]			
Cu1–N1	2.186(4)	Cu2–N2	2.040(4)
Cu1–N3	2.021(5)	Cu2–N4	2.348(6)
Cu1–Cu2	3.7942(2)	Cu1–Cu1	6.3283(3), 5.9223(3)
Cu2–Cu2	7.5885(3)		
β-[Cu(ta)$_2$]			
Cu1–N1	2.174(3)	Cu1–Cu2	3.7762(2)
Cu2–N2	2.317(9)	Cu1–Cu1	6.1665(4)
Cu2–Cu2	7.5524(4)		

equatorial Cu1–N_{eq} bonds (Cu1–N1, 2.19 Å) and two short apical Cu1–N_{ap} bonds (Cu1–N3, 2.02 Å) leading to flattened octahedra (green color). In contrast the Cu2 centers, placed at sites of $\bar{4}m2$ symmetry, have four short equatorial Cu2–N_{eq} bonds (Cu2–N2, 2.04 Å) and two long apical Cu2–N_{ap} bonds (Cu2–N4, 2.35 Å) (elongated red octahedra).

In contrast the Jahn–Teller distortion of the CuN_6 octahedra disappears completely in cubic β-[Cu(ta)$_2$]. However, according to the framework bonding topology (*cf.* Fig. 2), two different kinds of Cu(II) coordination sites still exist, which differ in terms of average Cu–N bond lengths. While the first octahedron (green colour in Fig. 5b) hosting the Cu1 atom at sites of $\bar{3}m$ symmetry, contains six short and equidistant bonds (Cu1–N1, 2.18 Å), the second Cu(II) site ($\bar{4}3m$ site symmetry, red octahedron) containing the Cu2 atom, bears six equidistant long copper–nitrogen bonds (Cu2–N2, 2.32 Å). The Cu–N bond lengths in both compounds fall within the expected range (2.021(5)–2.348(6)) and are in a good agreement with other copper–triazolate complexes (1.90–2.45 Å).[9a,c,15] In Table 1, selected bond lengths for α- and β-[Cu(ta)$_2$] are given. Atom coordinates, full list of bond lengths and angles for α- and β-[Cu(ta)$_2$] are collected in Tables S1–S4, ESI.†

Both compounds contain Kuratowski-type SBUs, as shown in Fig. 2. Within each SBU four Cu(II) ions occupy the vertices of an imaginary tetrahedron and the central Cu2 atom is coordinated to six triazolate ligands. In the case of β-[Cu(ta)$_2$], a perfect tetrahedron is observed (Cu1 atoms are placed at equal distances of 6.17 Å), whereas a distorted tetrahedron is observed in α-[Cu(ta)$_2$] (non-bonding Cu–Cu distances of 6.328 and 5.922 Å, respectively; see Fig. 5c and d).

α-[Cu(ta)$_2$] contains Cu(II) ions in the centres of Kuratowski units bound to the N^A donors of the ta^- ligands (*cf.* Fig. 6) and Cu(II) centres (constituting the peripheral metal centers of the original $K_{3,3}$ units) coordinated by the N^B donors of the ta^- ligand. A putative reaction scheme representing the formation of a [Cu(ta)$_2$] network by the stepwise polymerization of (lacunary) Kuratowski-type building units is shown in Fig. 6.

As mentioned before, there are two different kinds of Cu(II) centers in both [Cu(ta)$_2$] polymorphs. The Cu(II) ions bound to the triazolate N^A-donor atoms experience a ligand field strength, which is dissimilar to the ligand field imposed onto Cu(II) ions by the N^B donor atoms. The ligand field strength for $Cu(N^A)_6$ should be lower than for $Cu(N^B)_6$ because in [Cu(ta)$_2$] the nitrogen–metal bond lengths for the central atom are longer than the corresponding distances for the peripheral N–Cu bonds, similarly to other compounds with $K_{3,3}$ units.[11,16] The superposition

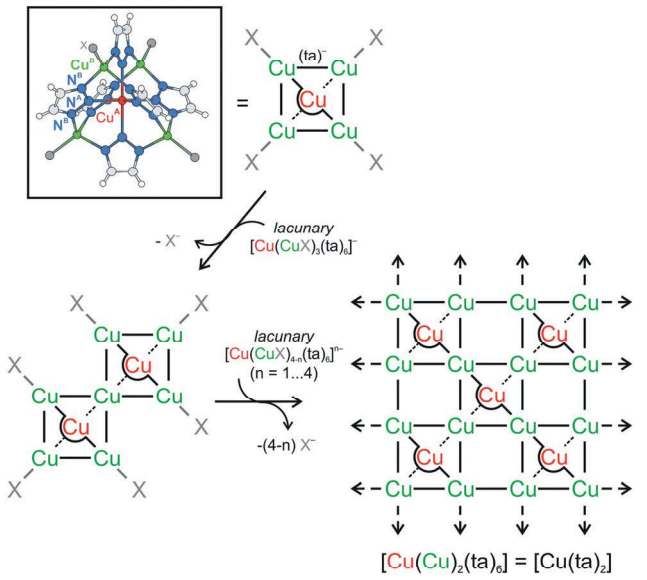

Fig. 6 Putative reaction scheme showing the formation of a $[Cu(ta)_2]$ network (*H*-ta = 1*H*-1,2,3-triazole) by stepwise polymerization of (lacunary) Kuratowski-type building units. The inset represents the ball-and-stick representation of a hypothetical Kuratowski coordination unit (chemical formula: $[Cu(CuX)_4(ta)_6]$ (X^- = anionic monodentate ligand, *e.g.* Cl^-, OH^-) which might serve as initiator of the polymerization process. The final compound $[Cu(ta)_2]$ contains octahedrally coordinated copper(II) centers which are different in terms of their nitrogen donor subsets (red: $\{Cu^A(N^A)_6\}$; green: $\{Cu^B(N^B)_6\}$, where N^A refers to the middle nitrogen atom of the 1,2,3-triazolate ring system"). Note that the structures of intermediate oligomeric species are largely unknown.

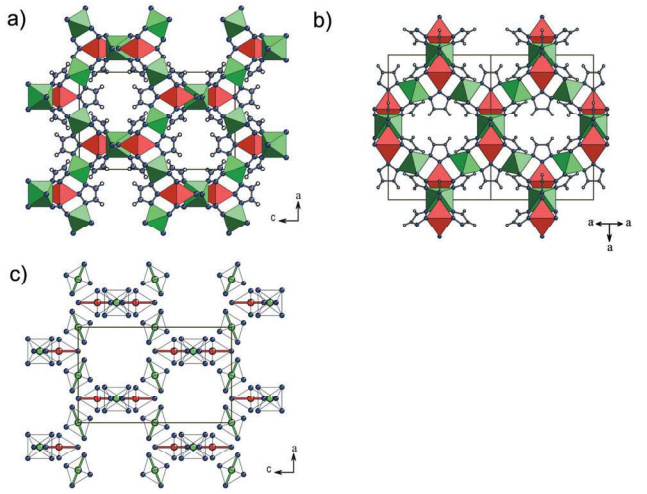

Fig. 7 Packing plots showing structural features of the coordination frameworks α- (a) and β-$[Cu(ta)_2]$ (b). Ball-and-stick representation including coordination polyhedrons of Cu(II) centers, (red polyhedrons: $Cu2\{(N4)_2(N2)_4\}$; green polyhedrons: $Cu1\{(N3)_2(N1)_4\}$). (c) Orientation of the Jahn–Teller distorted octahedra is given with respect to the crystallographic directions in α-$[Cu(ta)_2]$, view in direction [100].

of different ligand fields and different Cu(II) site symmetries leads to two different Jahn–Teller distortions in α-$[Cu(ta)_2]$. As shown in Fig. 7, tetragonal distortion leads to an elongation of the $\{N_6\}$ octahedron of Cu2 in the direction of an axis running through the atoms N4–Cu2–N4 (red axes), whereas a compression of the {N6} octahedron of Cu1 is observed in the direction of an axis running through the atoms N3–Cu1–N3 (green axes). Interestingly, red axes are uniformly co-aligned with the *c*-direction, whereas there are two subsets of compressed octahedra (green) which show Jahn–Teller distorted axes roughly coaligned either to the *a*- or the *b*-direction of the crystal lattice. The Jahn–Teller distortion disappears in the high temperature phase, β-$[Cu(ta)_2]$. However, the higher symmetric β-phase has still two different kinds of Cu(II) centers in the ratio 1 : 2, Cu2 to Cu1, because the bonding scheme does not change during the phase transition. The crystal packing diagrams of α- and β-$[Cu(ta)_2]$ in *y*- and *z*-direction are shown in Fig. S1a–b and Fig. S2a–b, ESI,† respectively.

The thermally induced reversible phase transition of $[Cu(ta)_2]$ from the room-temperature α- into the high-temperature β-phase leads to an elongation of Cu–N bonds, namely Cu1–N3 from 2.02 to 2.17 Å, and Cu2–N2 from 2.04 to 2.32 Å. As a result, two Cu(II) ions in β-$[Cu(ta)_2]$ are equidistantly surrounded by two different sets of nitrogen atoms, $(Cu1(N1)_6$ and $Cu2(N2)_6)$. This process is accompanied by a change of crystal system and space group from tetragonal, space group $I4_1/amd$ to the higher symmetric cubic lattice with space group $Fd\bar{3}m$, the former space group $I4_1/amd$ being a subgroup of $Fd\bar{3}m$.[17] In particular, the positions of Cu1 and Cu2 atoms change from sites of symmetry 2/*m* (Wyckoff position 8c) to $\bar{3}m$ (16c) in the case of Cu1 and from $\bar{4}m2$ (4a) to $\bar{4}3m$ (8a) for Cu2. Next, the positions of N4 (Wyckoff position 8e, site symmetry 2*mm*) and N2 (16g, 2) atoms (α-$[Cu(ta)_2]$) are joined into the position of N2 (48f, 2*mm*) atom in β-$[Cu(ta)_2]$. Similarly, the positions of N3 (16h, *m*), N1 (32i, 1) and C1 (16h, *m*), C2 (32i, 1) atoms in α-$[Cu(ta)_2]$ are joined into the positions of N1 (96g, *m*) and C1 (96g, *m*) atoms in β-$[Cu(ta)_2]$, respectively.

The crystal structure of α-$[Cu(ta)_2]$ contains 2D unidirectional hydrophobic channels flanked by hydrogen atoms stemming from triazolate ligands. A dense packing of copper coordination octahedra is observed in *c*-direction. Similar packing features are observed in the crystal structure of β-$[Cu(ta)_2]$, where the open channels are running along the [011] direction. The network topology of $[Cu(ta)_2]$ can be simplified by considering the imaginary Cu2-centered $Cu2(Cu1)_4$ tetrahedral units as 4-connected nodes. The resulting 4-connected diamond-like net (shown in Fig. 8 along the *a*-direction) can be represented by a 6^6 topological symbol.

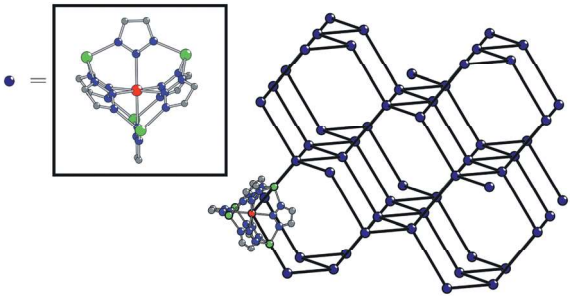

Fig. 8 The 6^6 diamond-like framework formed by 4-connected nodes (= Kuratowski units displayed in the inset figure) for α- and β-$[Cu(ta)_2]$.

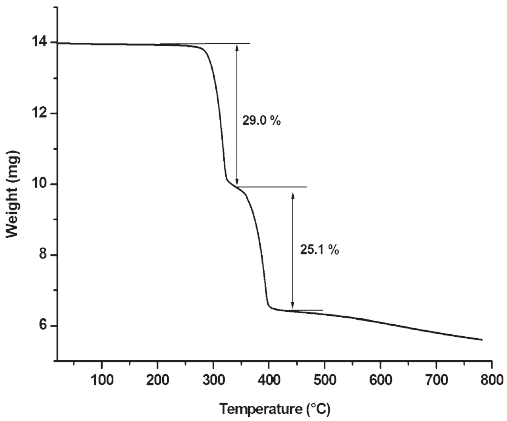

Fig. 9 Temperature-dependent weight-loss of the compound $[Cu(ta)_2]$ under flowing nitrogen gas.

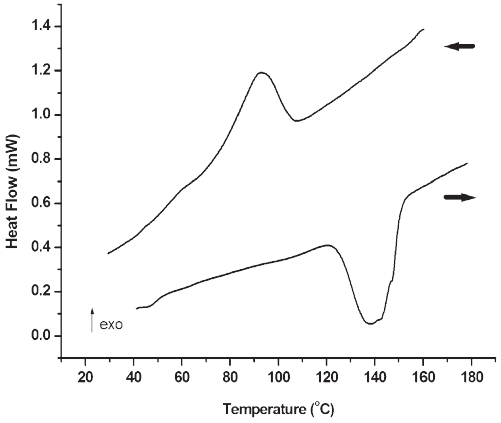

Fig. 10 DSC curves for $[Cu(ta)_2]$ registered with a scanning rate of 10 K min^{-1} at heating (lower curve) and cooling (upper curve).

TGA, DSC and VTXRPD studies. Phase purity of α-$[Cu(ta)_2]$ was confirmed by XRPD measurement at ambient conditions. The experimental XRPD pattern is consistent with the simulated one as gleaned from the single-crystal X-ray diffraction data (Fig. S3a–b, ESI†). For the characterization of thermal stability, TGA, DSC and variable temperature XRPD experiments were performed (Fig. 9–11). The thermogravimetric profile exhibits no weight loss until 280 °C, indicating that the freshly prepared compound had lost any occluded solvent molecule prior to TGA measurement. Two weight losses between room temperature and *ca.* 410 °C (29 %, 280–310 °C and 25.1 %, 310–410 °C) correspond to the gradual (two steps) pyrolitic decomposition of the compound $[Cu(ta)_2]$.

Differential scanning calorimetry (DSC) measurements for $[Cu(ta)_2]$ were performed in the temperature range 25–180 °C with a scanning rate of 10 K min^{-1}. Fig. 10 shows the temperature dependencies of the heat flows (DSC curves) obtained for $[Cu(ta)_2]$ on heating (lower curve) and on cooling (upper curve). Two anomalies on the DSC curves were registered. During the heating process an endothermic effect in the temperature range of 120–155 °C was observed. Next, during the cooling process an exothermic effect between 120 and 70 °C was detected. The endothermic maximum is connected with the phase transition of

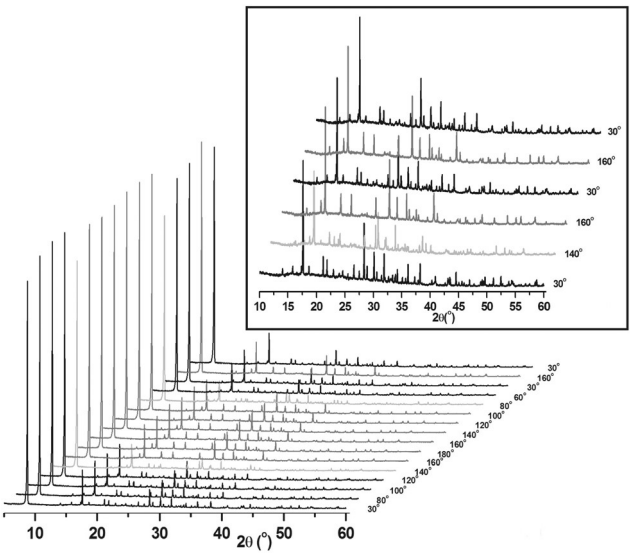

Fig. 11 VTXRPD plots in the range of 30–180–30 °C. For clarity, the inset shows an expanded view in the range 10–60° 2θ. Black line: α-$[Cu(ta)_2]$; grey: β-$[Cu(ta)_2]$; light grey: transition state.

compound α-$[Cu(ta)_2]$ to compound β-$[Cu(ta)_2]$ (ΔH = 1.67 kJ mol^{-1}, ΔS = 4.32 J mol^{-1} K^{-1}) and the exothermic one is connected with the reversible phase transition of β-$[Cu(ta)_2]$ to α-$[Cu(ta)_2]$ (ΔH = 1.68 kJ mol^{-1}, ΔS = 4.35 J mol^{-1} K^{-1}, T_c = 113 °C).

According to the XRPD data (Fig. 11), compound $[Cu(ta)_2]$ is stable up to at least 180 °C. The phase transition between compounds α- and β-$[Cu(ta)_2]$ occurs in a temperature range of 120–160 °C. The phase transition is fully reversible: after cooling β-$[Cu(ta)_2]$ transforms into α-$[Cu(ta)_2]$ in the temperature range 80–60 °C and the initial powder X-ray diffraction pattern is regained. These results are in a good agreement with the results obtained from DSC measurements. In order to further confirm the reversibility of the phase transition, the sample was cooled to 30 °C, after which it was heated to 160 °C again and the resulting powder X-ray diffraction patterns were compared. The intensities, positions and areas of the Bragg reflexes were identical in all cases (see Table S5, ESI†), which indicates that the structural transition is fully reversible. The intensities of the main peak centred at *ca.* 8.6° 2θ are clearly lower at the transition stages (140 and 80 °C, light grey patterns in Fig. 11) which is connected with the changes on atom coordinates.

Physisorption results

Compound α-$[Cu(ta)_2]$ exhibits permanent porosity, which was confirmed by argon gas sorption. Prior to measurement, the sample was degassed at 100 °C for 1 h in a high vacuum. The argon adsorption isotherm follows a type-I behaviour, typical for microporous solids and the maximum uptake achieved at 77 K and 1 bar is 179 cm^3 g^{-1} (Fig. 12). The micropore volume obtained from the sorption isotherm is 0.19 cm^3 g^{-1} using an NLDFT method.[18] The same value was obtained by using the t-method micropore analysis.[19] The adsorption data was fitted to the BET equation to give a surface area of 440 m^2 g^{-1}. This

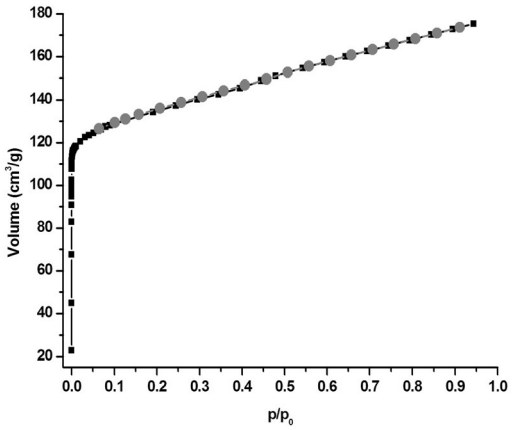

Fig. 12 Argon adsorption (black squares) and desorption (grey circles) isotherms measured for a desolvated sample of α-[Cu(ta)$_2$] at 77 K.

value is a little smaller than the theoretical surface area calculated from a Monte Carlo integration technique (where a probe molecule is 'rolled' over the surface), which is 570 m^2 g^{-1}.[20] An estimation with PLATON/SQUEEZE[21] reveals that the total potentially accessible void volume is 968.1 Å^3 or 0.24 cm^3 g^{-1} which is 36.4% of the unit cell volume (2662.6(3) Å^3). In the case of compound β-[Cu(ta)$_2$] the total potentially accessible void volume is 1671.1 Å^3 (0.21 cm^3 g^{-1}) or 31.5% of the unit cell volume (5305.9(8) Å^3). Thus, β-[Cu(ta)$_2$] has a smaller void volume due to a more dense packing. To evaluate the pore size distribution, the argon sorption isotherms sampled at 77 K were analyzed using non-local density functional theory (NLDFT) implementing a carbon equilibrium transition kernel for argon adsorption at 77 K based on a slit-pore model.[22] The distribution calculated by fitting the adsorption data reveals one kind of micropores with a diameter of 5.7 Å (Fig. 13). This value is found in good agreement with a pore diameter calculated from crystallographic data (5.1–6.5 Å, taking the van der Waals radii of 1.2 Å for H atoms into account). The pore width seems to be sufficiently large in order to occlude ethanol molecules, which have a kinetic diameter of 4.5 Å.[23] However, occluded solvent molecules are quickly lost upon isolation and work-up of the as-freshly prepared crystals, and thus α-[Cu(ta)$_2$] contains no solvent molecules.

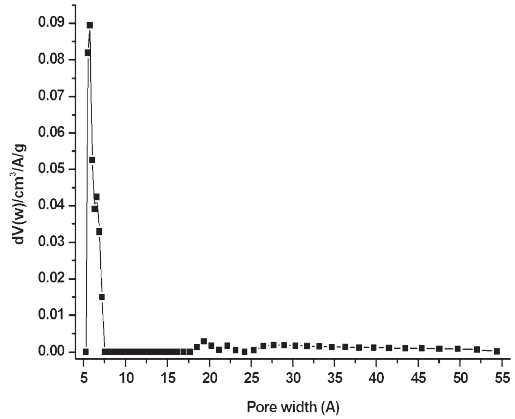

Fig. 13 Pore size distribution for compound α-[Cu(ta)$_2$] calculated by fitting a NLDFT model to the argon sorption data.

Fluorescence and UV-vis spectroscopy

Compound α-[Cu(ta)$_2$] shows blue-green fluorescent emission at room temperature. As shown in Fig. 14, upon excitation at 330 nm (dashed line), α-[Cu(ta)$_2$] displays a broad and featureless emission band in the visible region with a maximum at 440 nm, whereas the 1*H*-1,2,3-ta ligand shows an emission band with a maximum at 375 nm upon excitation at 319 nm. Thus, α-[Cu(ta)$_2$] exhibits a red-shifted emission, compared to the free ligand. This red-shift is typical for Cu(II) compounds, and it has been employed in the development of Cu^{2+} chemosensors.[24] The intensity of the emission band of α-[Cu(ta)$_2$] is significantly lower than that of the free ligand, which is consistent with a commonly observed quenching of fluorescence emission by Cu(II) ions.[25] The solid-state UV-vis spectrum of compound α-[Cu(ta)$_2$] (Fig. 15) displays one broad absorption peak in the visible region with a maximum at 650 nm, which is ascribed to the *d*–*d* transition of the Cu(II) ions. The second intense band at

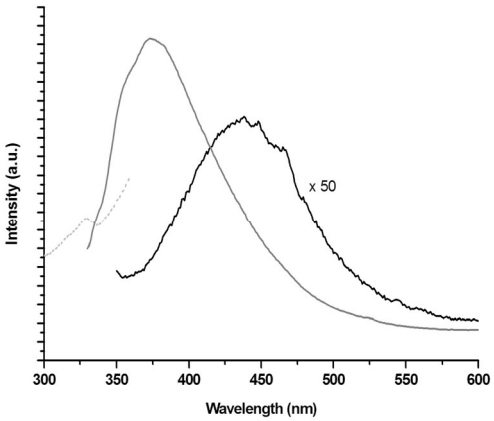

Fig. 14 Solid-state fluorescence spectra for α-[Cu(ta)$_2$] (black) and 1*H*-1,2,3-ta (grey) at room temperature. Dashed line (---) excitation. The intensity for α-[Cu(ta)$_2$] is multiplied by 50.

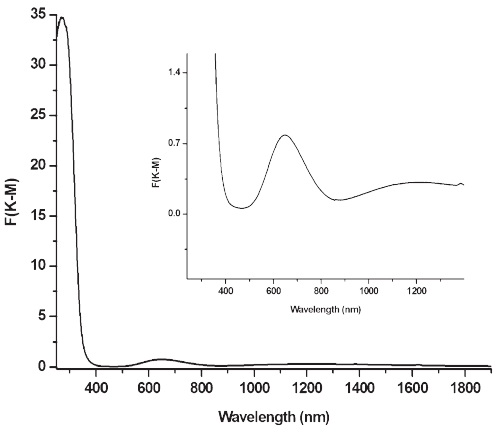

Fig. 15 UV-vis-NIR spectrum of α-[Cu(ta)$_2$] at room temperature.

270 nm observed in the UV range can be attributed to the intra-ligand transition.

Magnetic studies

Magnetic susceptibility measurements, $\chi(T)$, were performed studying a polycrystalline sample in a field of 1 T between 2–400 K. The molar susceptibility data are normalized to the formula unit (f.u.) of $Cu(N_3C_2H_2)_2$ and the molar core diamagnetism of $\chi_{dia} = -0.088$ memu mol^{-1} was subtracted from the data. The diamagnetic contribution χ_{dia} has been estimated by the expression $\chi_{dia} = -0.79 \times \Sigma_i Z_i \times (r/a_B)^2\ 10^{-6}$ emu mol^{-1}, where $\Sigma_i Z_i$ is the sum of all core electrons/f.u.; a_B is the Bohr radius and $(r/a_B)^2$ is assumed to be unity.

Fig. 16a reveals for α-[Cu(ta)$_2$] a linear dependence of $\chi^{-1}(T)$ *vs.* temperature above 150 K. Assuming a Curie–Weiss type relationship, $\chi = C/(T - \theta_P)$ yields a paramagnetic Curie temperature θ_P of −45 K and an effective moment of $\mu_{eff} = 1.9\ \mu_B$. This effective magnetic moment deviates slightly from the spin-only value associated with the presence of d^9 Cu-ions in α-[Cu(ta)$_2$], *i.e.*, $\mu_{eff} = 1.73\ \mu_B$, and hints for an enhanced averaged *g*-factor of $g = 2.2$ as a consequence of the Jahn–Teller distorted ligand-field at both crystallographically independent Cu(II) ions.

The magnetization curve $m(B)$ at $T = 2$ K is depicted in Fig. 16b, and can be well described by a Brillouin-function of a pure spin-1/2 system with $g = 2.2$ up to 7 T. However, the saturation magnetization of 0.31 μ_B/f.u. indicates that only one third of the paramagnetic moments of the Cu(II) ions contribute to the magnetic response at low temperatures. This finding suggests a scenario of two magnetically different Cu-sites in [Cu(ta)$_2$]: one third of the Cu-ions display a constant magnetic moment over the whole temperature range, whereas the magnetic moment of the remaining two thirds of Cu-ions is quenched at low temperatures. We note, that the ratio of 1 : 2 between the magnetically different Cu(II) sites is in agreement with the 1 : 2 ratio of the crystallographic Cu(2) and Cu(1) ions.

To shed more light on this puzzling behaviour we first calculate the effective magnetic moment from the linear behavior of the $\chi^{-1}(T)$ *vs.* T plot below 6 K (see Fig. 16). The resulting $\mu_{eff} = 1.06\ \mu_B$ is in line with above observation that only one third of the Cu-ions contribute to the magnetic moment. Here the concentration of the paramagnetic ions are calculated by $n = (\mu_{eff,[low\text{-}T]})^2/(\mu_{eff\ total})^2 = 0.31$ with $\mu_{eff[low\text{-}T]} = 1.06\ \mu_B$ and $\mu_{eff\ [total]} = 1.9\ \mu_B$. In the following these Cu(II) ions are denoted Cu(para) in line with their constant paramagnetic behaviour in the temperature range of 2–400 K. Furthermore, the remaining Cu(II) ions are denoted Cu(af) – since these are characterized by antiferromagnetic correlations. This finding is supported by the next step of our analysis, where we subtracted the magnetic contribution of the Cu(para)-ions from the total susceptibility data. The temperature dependence of the remaining susceptibility can be well described by a Bleaney and Bowers-type expression,[26] describing the antiferromagnetic coupling in dinuclear moieties: $\chi = 0.375 \times g^2/(T(3 + \exp[-J_E/T]))$ with $g = 2.2$ and $J = -88$ K, the exchange coupling parameter between the two paramagnetic moments (see Fig. 16c). As a result, two magnetically different Cu sites Cu(para) and Cu(af) in the ratio 1 : 2 can be identified in [Cu(ta)$_2$]. The observed ratio in the magnetic studies suggests that the Cu(para) and Cu(af) ions might be linked with the Cu2 and Cu1 positions, respectively. In case of the paramagnetic Cu(para) ions no magnetic correlations could be identified indicating by the vanishing of $\theta_p = 0$. The remaining Cu(af) sites are characterized by antiferromagnetic dimerization at low temperatures. However, at elevated temperatures the magnetic behaviour of the Cu(af) sites also follows a Curie–Weiss type-relation. The resulting effective moment of $\mu_{eff} = 1.6\ \mu_B$ is again consistent with a concentration of 0.71 which confirms the picture of two different Cu sites in [Cu(ta)$_2$] with an occupation ratio of roughly 2 : 1. A direct mapping of the Cu(para)- and Cu(af)-ions to the different crystallographic Cu(II) sites (Cu1 and Cu2) is not yet clear and has to be carefully examined in future. But a possible scenario may be, that the antiferromagnetic correlation is mediated by the three nitrogen atoms of the bridging triazolate ligands as has also been reported for $\mu_{1,3}$-azido bridged Ni atoms in di-Ni(II) complexes.[27]

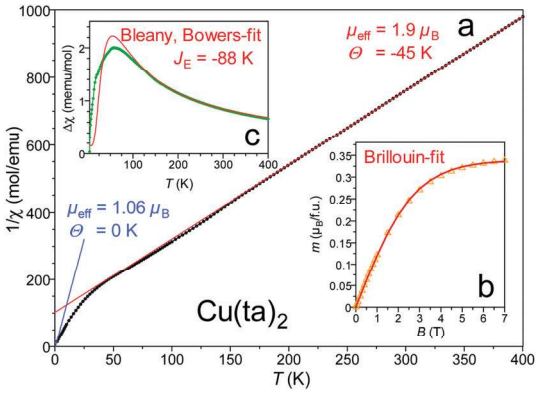

Fig. 16 (a) Temperature dependence of the inverse magnetic susceptibility at $B = 1$ T, (b) magnetization curve $m(B)$ at $T = 2$ K and (c) the temperature dependence of the susceptibility $\Delta\chi$ of the dinuclear contribution. All solid lines are fits to the data using the respective theoretical models as specified in the text.

Conclusions

The work reported here focuses on the synthesis and characterization of a novel Cu(II)-containing metal–organic framework comprised of fully condensed Kuratowski-type secondary building units. Its unique bond topology represents one of the three principally different strategies for assembling porous coordination frameworks from these building units. [Cu(ta)$_2$] exhibits high thermal stability and permanent porosity. Since the diamond-like network contains octahedrally coordinated metal(II) ions and 1,2,3-triazolate ligands only, a host of metal-substituted isotypic derivatives can be anticipated. The triazolate ligands give rise to strong electronic and magnetic exchange interactions of the metal centers. The residual flexibility of the framework allows for structural distortions, such as the large tetragonal Jahn–Teller distortion of $Cu^{II}N_6$ coordination sites. [Cu(ta)$_2$]-type frameworks bear two different metal coordination sites, which is dictated by the network topology. It should thus be possible to engineer functional homo- and bimetallic frameworks from suitable precursors, which gleans further support

from the fact that a range of heteropentanuclear Kuratowski complexes have been described previously.[10]

MOFs inherit the principle advantage of multi-functionality; in light of potential applications $[Cu(ta)_2]$-type frameworks might be tailored to exhibit a combination of porosity and stimulus-responsive properties, such as temperature- or pressure-dependent magnetic exchange interactions. It should be noted in this context that the compound $[Fe^{II}{}_3Zn_6Cl_6L_{12}]$ (L = 5,6-dimethoxy-1,2,3-benzotriazolate), which is a heterononanuclear dimer of condensed Kuratowski units, shows thermally induced spin-crossover.[28] Embedding Fe(II) centers in $[Cu(ta)_2]$-type frameworks might thus lead to robust compounds exhibiting stimulus responsive spin-crossover hysteresis, which could be employed in sensing or information processing applications. On the other hand, employing less symmetric 1,2,3-triazolate ligands might lead to a symmetry reduction in $[Cu(ta)_2]$ networks,[29] and the resulting compounds might display ferroelectric properties, that is spontaneous electric polarization.[30] Noteworthy, a first Cu(II)-containing MOF, which exhibits ferromagnetism coupled with ferroelectricity, has been described very recently.[31]

Experimental

Materials and general methods

All reagents were of analytical grade and used as obtained from commercial sources without further purification. Fourier transform infrared (FTIR) spectra were recorded in the range 4000–400 cm^{-1} on a Bruker Equinox 55 FT-IR spectrometer. The following indications are used to characterize absorption bands: very strong (vs), strong (s), medium (m), weak (w), very weak (vw). Elemental analyses (C, H, N) were carried out on a Perkin-Elmer 2400 Elemental Analyzer. Thermogravimetric analysis (TGA) was performed with a TGA Q500 analyzer in a temperature range of 25–800 °C in flowing nitrogen at a heating rate of 10 °C min^{-1}. DSC measurements were carried out on a DSC 2920 Modulated DSC with Refrigerated Cooling System TA Instruments apparatus in a temperature range of 25–180 °C. The enthalpy change (ΔH) was calculated by the numerical integration of the DSC curve under the peak after linear background arbitrary subtraction. The entropy change (ΔS) was calculated using the formula $\Delta S = \Delta H\ T_c^{-1}$. Ambient temperature X-ray powder diffraction (XRPD) patterns were measured using a Seifert XRD 3003 TT diffractometer with Meteor 1D detector operated at 40 kV, 40 mA for Cu target (λ = 1.54178 Å) with a scan speed of 10 s $step^{-1}$ and a step size of 0.02° 2θ. Variable temperature X-ray powder diffraction (VTXRD) measurements were performed in a capillary at a temperature range from 30 to 230 °C with a Bruker D8 Advance diffractometer equipped with an mri TCPU1 reaction chamber, operating in transmission geometry. The heating rate between temperatures was 0.5 °C min^{-1}. The sample was heated at each temperature for 10 min and the patterns were recorded in the 6–75° 2θ range, with 0.4 s time $step^{-1}$, and a step width of 0.02° in 2θ. XRPD measurement for the crystal structure determination was collected using a PANalytical XPERT PRO MPD diffractometer equipped with PIXcel detector, Anton Paar HTK-1200N oven. The argon sorption isotherms at −196 °C up to 1 bar were measured using a Quantachrome Autosorb-1C apparatus. High purity gas was used for the adsorption experiments (argon 99.999%). The UV/VIS spectrum was recorded on Perkin-Elmer Lambda 750S spectrometer in the range of 250–2000 nm with a lamp change at 320 nm. The luminescence spectrum was acquired with Fluoro-Max-4 Spectrofluorometer at room temperature. The excitation and emission spectra were corrected for the wavelength-dependent lamp intensity and detector response, respectively. The magnetic measurements were performed in the temperature range between 1.8 and 400 K and in magnetic fields up to 7 T using a Quantum Design MPMS7 superconducting quantum interference device (SQUID) magnetometer.

Synthesis of α-$[Cu(ta)_2]$

A mixture of $Cu(OH)_2$ (0.06 mmol, 15 mg), Htz (1H-1,2,3-triazole) (0.31 mmol, 21 mg), $NH_{3(aq)}$ (25 %, 2 mL) and EtOH (2 mL) was placed in a glass tube (16 mL). The tube was sealed and heated at 120 °C for two days. The reaction mixture was slowly cooled to room temperature. Blue crystal of α-$[Cu(ta)_2]$ suitable for single crystal X-ray diffraction analysis were picked up from the mother liquid and the light-blue crystalline solid was filtered off, washed thoroughly with EtOH and dried in air. (Yield: 39%, 8.2 mg, based on ligand). C, H, N elemental analysis for $C_4H_4N_6Cu$: calcd: C: 24.06; H: 2.02; N: 42.09 (%); found: C: 24.19; H: 1.60; N: 40.06 (%). IR (cm^{-1}): 3145 (vw), 1721 (vw), 1652 (vw), 1472 (vw), 1457 (vw), 1422 (w), 1240 (w), 1218 (m), 1192 (m), 1110 (vs), 1102 (s), 996 (w), 979 (m), 970 (s), 864 (vw), 794 (vs), 718 (m), 663 (vw), IR spectrum is shown in Fig. S4, ESI.†

X-ray data collection and structure determination-single crystal analysis

Single crystal x-ray diffraction. X-ray data for the crystal structure determination of α-$[Cu(ta)_2]$ were collected on a Bruker APEX-II four-circle diffractometer with κ-geometry, equipped with a CCD camera. The structure was solved by direct methods and refined with the SHELXL[32] program package using weighted full-matrix least squares on F^2. All non-hydrogen atoms were refined anisotropically. Hydrogen atoms were placed in idealized positions and included as riding atoms with a distance constraint of d(C–H) = 0.97 Å. In spite of the porous structure, no additional electron density in accessible voids has been detected. Therefore SQUEEZE procedure was not applied. The crystal data and refinement details for compound α-$[Cu(ta)_2]$ are listed in the Table 2.

Powder X-ray diffraction structure analysis

A microcrystalline sample was gently ground using an agate mortar and pestle, and was deposited in the hollow of a corundum sample holder of a high temperature camera. Diffraction data were collected at 200 °C in the 2θ range of 5–90° with 0.02° steps, with a scan speed 900 s $step^{-1}$ using a PANalytical XPERT PRO MPD diffractometer equipped with PIXcel detector, Anton Paar HTK-1200N oven, optics: primary beam Soller slits 4°, fixed divergence slit 1/2°, receiving slit 1/2°, reflection

Table 2 Crystal data and structure refinement summary for α- and β-[Cu(ta)$_2$] compounds

Compound	α-[Cu(ta)$_2$]	β-[Cu(ta)$_2$]
Diffractometer	Bruker APEX–II	PANalytical XPERT PRO MPD
X-ray source/wavelength/Å	Mo, 0.71073	Cu, 1.5425
T/K	295(2)	473(3)
Empirical formula	$Cu(C_4N_6H_4)_2$	$Cu(C_4N_6H_4)_2$
Formula	$C_4H_4N_6Cu$	$C_{12}H_{12}Cu_3N_{18}$
M_r	199.67	599
Crystal system	Tetragonal	Cubic
Space group	$I4_1/amd$ (no. 141)	$Fd\bar{3}m$ (no. 227)
a/Å	11.8447(7)	17.4416(15)
c/Å	18.9782(13)	—
V/Å^3	2662.6(3)	5305.9(8)
Z	12	8
D_c/g cm^{-3}	1.494	1.4689
μ/mm^{-1}	2.409	3.055
F(000)	1188	2280
Crystal size/mm	0.04 × 0.04 × 0.01	Blue powder
θ Range/°, XRPD: 2θ range/°	3.24–28.54	8.22–90.00
Refls. total	20 893	—
Refls. unique	928	—
$R_{int.}$	0.1713	—
R_1 ($I > 2\sigma(I)$)[a]	0.0475	—
wR_2 (all data)[b]	0.1040	—
GooF	1.088	4.08
Number of observation	—	4089
M_{30}	—	58.50
F_{30}	—	69.75
R_{wp}	—	7.32
R_P	—	4.64
Data/restraints/parameters	928/0/47	24/4/16
Largest diff. peak and hole/Å^{-3}	0.507 and −0.605	—

[a] $R_1 = \Sigma||F_0| - |F_c||/\Sigma|F_0|$. [b] $wR_2 = \Sigma[w(F_0^2 - F_c^2)^2]/\Sigma[w(F_0^2)^2]^{1/2}$.

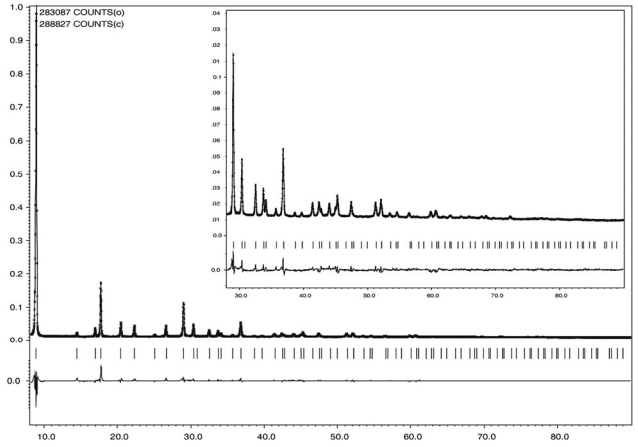

Fig. 17 The Rietveld refinement plots for β-[Cu(ta)$_2$]. Dotted and solid lines represent observed and calculated patterns, respectively with peak markers and the difference plot shown at the bottom. XRPD data were collected at 200 °C. For clarity, the inset shows an expanded view in the range 28–90° 2θ.

geometry. The generator was set at 40 kV, 30 mA. Extractions of the peak positions, pattern indexing, determining and refinement of the lattice parameters for β-[Cu(ta)$_2$] were carried out with PROSZKI package.[33] Independently, the indexing process was performed by N-TREOR09 program implemented in EXPO2009 package.[34] Space group determination by probabilistic approach was performed by using EXPO2009. The set of the most probable space groups was found: extinction group $Fd\_\_$, space groups $Fd\bar{3}$ (203), $Fd\bar{3}m$ (227). The $Fd\bar{3}m$ space group was chosen for further structure determination procedures. During pattern decomposition the lattice parameters were not refined. The positions of all atoms were found by direct method. The hydrogen atom was placed in the idealized position by the SHELXL program. The Rietveld refinement was carried out using the Jana2006 program.[35] Weak geometric restraints on bond lengths were used during the refinement process. Experimental details and crystal data for β-[Cu(ta)$_2$] are listed in Table 2. The final Rietveld refinement plots are presented in Fig. 17.

Acknowledgements

This work was supported by the German Research Foundation (DFG) within Priority Program 1362. The authors thank Prof. Wiesław Łasocha (Faculty of Chemistry, Jagiellonian University, Poland) for the opportunity to perform XPRD measurements in a XRK Reactor Chamber.

Notes and references

1 (*a*) C. Banglin, X. Shengchang and Q. Guodong, *Acc. Chem. Res.*, 2010, **43**, 1115; (*b*) A. Dailly and E. Poirier, *Energy Environ. Sci.*, 2011, **4**, 3527; (*c*) L. J. Murray, M. Dincă and J. R. Long, *Chem. Soc. Rev.*, 2009, **38**, 1294.

2 (*a*) S. Qiu and G. Zhu, *Coord. Chem. Rev.*, 2009, **253**, 2891; (*b*) A. U. Czaja, N. Trukhan and U. Müller, *Chem. Soc. Rev.*, 2009, **38**, 1284; (*c*) J. R. Li, R. J. Kuppler and H. C. Zhou, *Chem. Soc. Rev.*, 2009, **38**, 1477; (*d*) E. Q. Procopio, F. Linares, C. Montoro, V. Colombo, A. Maspero, E. Barea and J. A. R. Navarro, *Angew. Chem., Int. Ed.*, 2010, **49**, 7308.

3 (*a*) S. T. Meek, J. A. Greathouse and M. D. Allendorf, *Adv. Mater.*, 2011, **23**, 249; (*b*) J. Y. Lee, O. K. Farha, J. Roberts, K. A. Scheidt, S. B. T. Nguyen and J. T. Hupp, *Chem. Soc. Rev.*, 2009, **38**, 1450.

4 M. Tonigold, Y. Lu, A. Mavrandonakis, A. Puls, R. Staudt, J. Möllmer, J. Sauer and D. Volkmer, *Chem.–Eur. J.*, 2011, **17**, 8671.

5 (*a*) S. Keskin and S. Kızılel, *Ind. Eng. Chem. Res.*, 2011, **50**, 1799; (*b*) E. Q. Procopio, S. Rojas, N. M. Padial, S. Galli, N. Masciocchi, F. Linares, D. Miguel, J. E. Oltra, J. A. R. Navarro and E. Barea, *Chem. Commun.*, 2011, **47**, 11751; (*c*) P. Horcajada, C. Serre, M. Vallet-Regi, M. Sebban, F. Taulelle and G. Férey, *Angew. Chem., Int. Ed.*, 2006, **45**, 5974; (*d*) R. C. Huxford, J. D. Rocca and W. Lin, *Curr. Opin. Chem. Biol.*, 2010, **14**, 262; (*e*) P. Horcajada, C. Serre, G. Maurin, N. A. Ramsahye, F. Balas, M. Vallet-Regí, M. Sebban, F. Taulelle and G. Férey, *J. Am. Chem. Soc.*, 2008, **130**, 6774; (*f*) J. An, S. J. Geib and N. L. Rosi, *J. Am. Chem. Soc.*, 2009, **131**, 8376.

6 S. Ferrer, J. G. Haasnoot, J. Reedijk, E. Müller, M. B. Cingi, M. Lanfranchi, A. M. M. Lanfredi and J. Ribas, *Inorg. Chem.*, 2000, **39**, 1859.

7 (*a*) J. P. Zhang, Y. Y. Lin, X. C. Huang and X. M. Chen, *J. Am. Chem. Soc.*, 2005, **127**, 5495; (*b*) J. P. Zhang, Y. B. Zhang, J. B. Lin and X. M. Chen, *Chem. Rev.*, 2012, **112**, 1001.

8 V. Colombo, S. Galli, H. J. Choi, G. D. Han, A. Maspero, G. Palmisano, N. Masciocchi and J. R. Long, *Chem. Sci.*, 2011, **2**, 1311.

9 (*a*) J. Chuang, W. Ouellette and J. Zubieta, *Inorg. Chim. Acta*, 2008, **361**, 2357; (*b*) M. C. Hu, Y. Wang, Q. G. Zhai, S. N. Li, Y. C. Jiang and Y. Zhang, *Inorg. Chem.*, 2009, **48**, 1449; (*c*) R. N. Devi, P. Rabu, V. O. Golub, C. J. O'Connor and J. Zubieta, *Solid State Sci.*, 2002, **4**, 1095; (*d*) V. Tangoulis, C. P. Raptopoulou, V. Psycharis, A. Terzis, K. Skorda, S. P. Perlepes, O. Cador, O. Kahn and E. G. Bakalbassis, *Inorg. Chem.*, 2000, **39**, 2522; (*e*) X. Gao, Q. G. Zhai, X. Dui, S. N. Li, Y. C. Jiang and M. C. Hu, *J. Coord. Chem.*, 2010, **63**, 214; (*f*) L. F. Jones, L. O'Dea, D. A. Offermann, P. Jensen, B. Moubaraki and K. S. Murray, *Polyhedron*, 2006, **25**, 360; (*g*) L. L. Li, H. X. Li, Z. G. Ren, D. Liu, Y. Chen, Y. Zhang and J. P. Lang, *Dalton Trans.*, 2009, 8567.

10 S. Biswas, M. Tonigold, M. Speldrich, P. Kögerler, M. Weil and D. Volkmer, *Inorg. Chem.*, 2010, **49**, 7424.

11 (*a*) D. Denysenko, M. Grzywa, M. Tonigold, B. Streppel, I. Krkljus, M. Hirscher, E. Mugnaioli, U. Kolb, J. Hanss and D. Volkmer, *Chem.–Eur. J.*, 2011, **17**, 1837; (*b*) S. Biswas, M. Grzywa, H. P. Nayek, S. Dehnen, I. Senkovska, S. Kaskel and D. Volkmer, *Dalton Trans.*, 2009, 6487.

12 C. Kuratowski, *Fund. Mat.*, 1930, **15**, 271.

13 Y. L. Bai, J. Tao, R. B. Huang and L. S. Zheng, *Angew. Chem., Int. Ed.*, 2008, **47**, 5344.

14 X. H. Zhou, Y. H. Peng, X. D. Du, J. L. Zuo and X. Z. You, *CrystEngComm*, 2009, **11**, 1964.

15 (*a*) J. Wang, M. Yu, Y. Yang, S. Zhang and F. Miao, *Chin. Sci. Bull.*, 2002, **47**, 890; (*b*) M. Murrie, D. Collison, C. D. Garner, M. Helliwell, P. A. Tasker and S. S. Turner, *Polyhedron*, 1998, **17**, 3031; (*c*) Y. Gong, X. H. Huang, Z. N. Xia, M. X. Gao and H. L. Zheng, *Acta Crystallogr., Sect. E: Struct. Rep. Online*, 2007, **63**, 216; (*d*) E. A. Goreshnik, D. Schollmeyer and M. G. Mys'kiv, *Z. Anorg. Allg. Chem.*, 2005, **631**, 835.

16 S. Biswas, M. Tonigold and D. Volkmer, *Z. Anorg. Allg. Chem.*, 2008, **634**, 2532.

17 H. Wondratschek and U. Müller, *International Tables for Crystallography*, 2004, vol. A1.

18 (*a*) P. I. Ravikovitch and A. V. Neimark, *Colloids Surf.*, 2001, **11**, 187–188; (*b*) S. J. Gregg and K. S. W. Sing, *Adsorption in Surface Area and Porosity, London*, Academic Press, UK, 1982, p. 42.

19 F. Rouquerol, J. Rouquerol and K. Sing, *Adsorption by Powders & Porous Solids*, Academic Press. San Diego, 1999.

20 (*a*) T. Düren, F. Millange, G. Férey, K. S. Walton and R. Q. Snurr, *J. Phys. Chem. C*, 2007, **111**, 15350; (*b*) K. S. Walton and R. Q. Snurr, *J. Am. Chem. Soc.*, 2007, **129**, 1578.

21 A. L. Spek, *J. Appl. Crystallogr.*, 2003, **36**, 7.

22 J. Jagiello and M. Thommes, *Carbon*, 2004, **42**, 1227.

23 L. Gales, A. Mendes and C. Costa, *Carbon*, 2000, **38**, 1083.

24 Z. Xu, X. Qian and J. Cui, *Org. Lett.*, 2005, **7**, 3029.

25 Z. Xu, Y. Xiao, X. Qian, J. Cui and D. Cui, *Org. Lett.*, 2005, **7**, 889.

26 B. Bleaney and K. D. Bowers, *Proc. Roy. Soc. (London)*, 1952, **Ser. A 214**, 451.

27 G. Leibeling, S. Demeshko, S. Dechert and F. Meyer, *Angew. Chem., Int. Ed.*, 2005, **44**, 7111.

28 S. Biswas, M. Tonigold, H. Kelm, H. J. Krüger and D. Volkmer, *Dalton Trans.*, 2010, **39**, 9851.

29 X. He, Z. X. Wang, F. F. Xing and M. X. Li, *Inorg. Chem. Commun.*, 2010, **13**, 417.

30 W. Zhang and R. G. Xiong, *Chem. Rev.*, 2011, 1163.

31 A. Stroppa, P. Jain, P. Barone, M. Marsman, J. M. Perez-Mato, A. K. Cheetham, H. W. Kroto and S. Picozzi, *Angew. Chem., Int. Ed.*, 2011, **50**, 5847.

32 G. Sheldrick, *Acta Crystallogr.*, 2008, **A 64**, 112.

33 W. Łasocha and K. Lewinski, *J. Appl. Crystallogr.*, 1994, **27**, 437.

34 A. Altomare, M. Camalli, C. Cuocci, C. Giacovazzo, A. Moliterni and R. Rizzi, *J. Appl. Crystallogr.*, 2009, **42**, 1197.

35 V. Petricek, M. Dusek and L. Palatinus, *Jana2006. The crystallographic computing System*. Institute of Physics, Praha, Czech Republic, 2006.